Dust-driven changes in particle pH differentially regulate secondary inorganic aerosol formation in central China

Hongyu Zhang[1, 2], Yating Zhang[1, 2], Yang Xiao[1, 2], Xiaohui Bi[1, 2]*, Shenbo Wang[3]*, Qili Dai[1, 2], Yinchang Feng[1,2]

[1] Key Laboratory of Urban Air Particulate Pollution Prevention and Control of Ministry of Ecology and Environment, College of Environmental Science and Engineering, Nankai University, Tianjin 300350, China

[2] CMA-NKU Cooperative Laboratory for Atmospheric Environment-Health Research, Tianjin 300350, China

[3] Research Institute of Environmental Sciences, Zhengzhou University, Zhengzhou 450000, China

* Corresponding authors: Xiaohui Bi and Shenbo Wang

E-mail address: bixh @nankai.edu.cn and shbwang@zzu.edu.cn

Text S1. Instruments

A Monitor for AeRosols and Gases in ambient Air (MARGA, Metrohm, Switzerland) was deployed at each observation site in Henan Province to continuously measure water-soluble inorganic ions (Na^+, NH_4^+, K^+, Mg^{2+}, Ca^{2+}, Cl^-, NO_3^-, and SO_4^{2-}) and trace gases (NH_3, HCl, and HONO). The MARGA system has been widely used in previous field studies (Li et al., 2017; Shi et al., 2017; Wang et al., 2019), and detailed descriptions of the instrument can be found in Markovic et al. (2012) and Rumsey et al. (2014). The system consists of three modules: a sampling module, an analytical module, and a data acquisition module. Ambient air first passed through a cyclone inlet at a flow rate of 16.7 L min^{-1} and then entered the sampling module at 3 L min^{-1}. Particles and gaseous pollutants were separated using a wet parallel-plate denuder or a wet rotating denuder, and were subsequently analyzed by two ion chromatography systems (Dionex Aquion, Dionex, USA).

Organic carbon (OC) and elemental carbon (EC) were measured using a semi-continuous carbon analyzer (Model-4, Sunset Laboratory, USA). Detailed information on this instrument is available in Panteliadis et al. (2014). The thermal-optical transmittance analysis of quartz filter samples was performed based on the NIOSH-5040 protocol. Carbon detected under a pure He atmosphere was defined as OC, whereas carbon oxidized under a mixed atmosphere of 90% He and 10% O_2 was defined as EC. Inorganic elements were measured using an X-ray fluorescence analyzer (Xact-625, Cooper Environmental Services, USA). Ambient particles passed through a $PM_{2.5}$ inlet and were collected on a Teflon filter tape. After approximately 1 h of sampling, the filter spot was moved to the analysis position, where elemental concentrations were determined by X-ray fluorescence and then converted to concentrations for the corresponding sampling period using the data processing software. $PM_{2.5}$ and PM_{10} mass concentrations were measured using two tapered element oscillating

microbalance instruments (Model 1400a and Model 1405, Thermo Electron, USA). Trace gases, including O_3, SO_2, NO_2, and CO, were obtained from a series of online analyzers (Thermo Electron, models 49i, 43i, 42i, and 48i, respectively) with a time resolution of 1 h. According to the instrument manuals, the precisions of the TE-49i and TE-42i analyzers are 1 ppb and 4 ppb, respectively. Meteorological parameters, including wind speed (WS), temperature (T), relative humidity (RH), and pressure (Pre), were measured simultaneously using an automatic weather station (LUFFT-WS500, Sutron Corporation, Germany), with accuracies of 0.1 m/s, ±0.2 °C, ±2%, and ±0.5 hPa, respectively.

Strict quality control procedures were applied throughout the sampling period to avoid potential contamination and ensure data reliability. For the analysis of water-soluble inorganic ions, calibration curves were established every two weeks to ensure accurate retention times and detector responses, with correlation coefficients higher than 0.999 for all target ions. Instrument components and sampling flow rates were also regularly replaced, checked, and calibrated. The method detection limits ranged from 0.002 μg/m^3 for Cl^- to 0.081 μg/m^3 for NH_4^+. For the MARGA measurements, Song et al. (2018) reported an overall relative uncertainty of 20% for the major species. Rumsey et al. (2014) reported analytical biases lower than 10% for SO_4^{2-}, NO_3^-, and higher than 15% for NH_3 and NH_4^+. Previous studies also showed good agreement between HONO measured by this ion monitoring system and that measured by a stripping coil-UV/visible absorption photometry (SC-AP) system (VandenBoer et al., 2014). Accordingly, the overall uncertainties were estimated to be 20% for NH_3 and NH_4^+ and 10% for the other species. Routine maintenance of the XRF analyzer included daily automatic QA checks, flow calibration, blank filter tests, and standard filter calibration to optimize instrument performance and ensure data accuracy. The detection limits ranged from 0.063 ng/m^3 for As to 100 ng/m^3 for Al. For the online OC/EC analyzer, automatic optical correction and sucrose calibration were performed

regularly, and instrument blanks were measured twice per day at 00:00 and 12:00. The precision of repeated measurements was better than 5%. The relative measurement uncertainty of the instrument was estimated to be 20% (Liu et al., 2013; Healy et al., 2013).

Text S2. Calculating for sulfate production rates

Aqueous-phase oxidation of SO_2 involves several pathways, including oxidation by O_3, and NO_2, transition metal ion (TMI)-catalyzed oxidation, methyl hydroperoxide oxidation, and peracetic acid oxidation. The sulfate production rates of aqueous-phase reaction, such as S(IV) oxidation by O_3, TMI, and NO_2, were calculated by referring to Seinfeld and Pandis, (2006) and Cheng et al. (2016).

Table S1. Rate expression and rate coefficients of relevant aqueous-phase reactions

Oxidants	Equations	Rate Expression (-d[S(IV)]/dt)
O_3	$S(IV) + O_3 \rightarrow S(VI) + O_2$	$(k_3[SO_2\cdot H_2O]+k_4[HSO_3^-]+k_5[SO_3^{2-}])[O_3(aq)]$ $k_3 = 2.4\times10^4\ M^{-1}s^{-1}$ $k_4 = 3.7\times10^5\ M^{-1}s^{-1}$, E/R= 5530 K $k_5 = 1.5\times10^9\ M^{-1}s^{-1}$, E/R= 5280 K
NO_2	$HSO_3^- + 2NO_2 \xrightarrow{H_2O} SO_4^{2-} + 3H^+ + 2NO_2^-$ $SO_3^{2-} + 2NO_2 \xrightarrow{H_2O} SO_4^{2-} + 2H^+ + 2NO_2^-$	$k_6[NO_2(aq)][S(IV)]$ pH < 5 $k_6 = (1.4\times10^5+1.24\times10^7)/2\ M^{-1}s^{-1}$ 5 < pH < 5.3 $k_6 = (23.25\times(pH-5)+1.4+124)/2\times10^5\ M^{-1}s^{-1}$ 5.3 < pH < 5.8 $k_6 = (23.25\times(pH-5)+1.4+12.6\times(pH-5.3)+124)/2\times10^5\ M^{-1}s^{-1}$ 5.8 < pH < 8.7 $k_6 = (12.6\times(pH-5.3)+124+20)/2\times10^5\ M^{-1}s^{-1}$ pH > 8.7 $k_6 = (2\times10^6+1.67\times10^7)/2\ M^{-1}s^{-1}$
TMI[a]+O_2	$S(IV) + \frac{1}{2}O_2 \xrightarrow{Mn^{2+},\ Fe^{3+}} S(VI)$	pH ≤ 4.2, $k_7[H^+]^{-0.74}$[Mn(II)]Fe(III)][S(IV)] $k_7 = 3.72\times10^7\ M^{-1}s^{-1}$ pH > 4.2, $k_8[H^+]^{0.67}$[Mn(II)]Fe(III)][S(IV)] $k_8 = 2.51\times10^{13}\ M^{-1}s^{-1}$

[a] The concentrations of Fe(III) and Mn(II) entirely depended on the values of pH due to the precipitation equilibriums of $Fe(OH)_3$ 和 $Mn(OH)_2$:

$$[\mathrm{Fe(III)}] = \frac{K_{sp,Fe(OH)_3}}{[OH^-]^3} \quad \text{and} \quad [\mathrm{Mn(II)}] = \frac{K_{sp,Mn(OH)_2}}{[OH^-]^2} \tag{1}$$

Where $K_{sp, Fe(OH)3}$ and $K_{sp, Mn(OH)2}$ are the precipitation constants of $Fe(OH)_3$ and $Mn(OH)_2$, respectively. The corresponding precipitation constant at 298K is 2.6×10^{-38} for $Fe(OH)_3$ and 1.6×10^{-13} for $Mn(OH)_2$.

In the above calculation formulas, the concentration of gas in the liquid is determined by Henry's constant (H^*). The calculation formula is as follows:

Table S2. Constants for calculating the apparent Henry's constant (H*).

Equilibrium	H (M atm^{-1}) at 298K	$-\triangle H_{298K}/R$ (K)
$SO_2(g) \leftrightarrow SO_2(aq)$	1.23	3145.3
$O_3(g) \leftrightarrow O_3(aq)$	1.10E-02	2536.4
$NO_2(g) \leftrightarrow NO_2(aq)$	1.00E-02	2516.2

SO_2 has a dissociation equilibrium in the solution, producing HSO_3^- and SO_3^{2-}. The ionization constants (K) are shown in the following table:

Table S3. Constants for calculating the ionization constants (K).

Equilibrium	K (M) at 298K	$-\triangle H_{298K}/R$ (K)
$SO_2{\cdot}H_2O \leftrightarrow H^+ + HSO_3^-$	1.30E-02	1960
$HSO_3^- \leftrightarrow H^+ + SO_3^{2-}$	6.60E-08	1500

The H* and K are temperature-dependent. The values are given in Table S3 and S4 under the condition of 298K, converted to the value under the actual temperature using the following calculation formula:

$$H(T)\ or\ K(T) = H(T_{298K})\ or\ K(T_{298K}) \exp\left[-\frac{\triangle H_{298K}}{R}\left(\frac{1}{T} - \frac{1}{298K}\right)\right] \tag{2}$$

Where $H(T)$、$K(T)$、$H(T_{298K})$, and $K(T_{298K})$ represent the H* and K at actual temperature and 298 K, respectively.

Influences of ionic strength on aqueous sulfate-producing rates were not considered because of the high values predicted by the ISORROPIA-II model during the sampling periods (Cheng et al., 2016). To evaluate the effects of mass transport, the formulation of a standard resistance model was adopted:

$$\frac{1}{R_{\mathrm{H,aq}}} = \frac{1}{R_{\mathrm{aq}}} + \frac{1}{J_{\mathrm{aq,lim}}} \quad (3)$$

Where $R_{H,\,aq}$ is the sulfate production rate, R_{aq} is the aqueous-phase reaction rate, and $J_{aq,lim}$ is the limiting mass transfer rate. which could be calculated by the formulas as follows:

$$J_{\mathrm{aq,lim}} = \min\{J_{\mathrm{aq}}(\mathrm{SO_2}),\, J_{\mathrm{aq}}(\mathrm{X})\} \quad (4)$$

$$J_{\mathrm{aq}}(\mathrm{X}) = k_{\mathrm{MT}}(\mathrm{X})\cdot[\mathrm{X}] \quad (5)$$

Where *[X]* refers to the aqueous-phase concentrations of SO_2 or the oxidants O_{xi} calculated by the equation in Table S2. The mass transfer rate coefficient $k_{mt(X)}$ (s^{-1}) can be calculated by:

$$k_{\mathrm{MT}} = [\frac{R_{\mathrm{p}}^2}{3D_{\mathrm{g}}} + \frac{4R_{\mathrm{p}}}{3\alpha\nu}]^{-1} \quad (6)$$

Where R_p is the aerosol radius, D_g is the gas-phase molecular diffusion coefficient (0.2 $cm^2\ s^{-1}$ at 293K), v is the mean molecular speed of X (3×10^4 cm s^{-1}), and a is the mass accommodation of X on the droplet surface, and we adopted values of 0.11, 0.23, 2.0E-3, and 2E-4 for SO_2, H_2O_2, O_3, and NO_2, respectively referring to Cheng et al. (2016).

Figures.

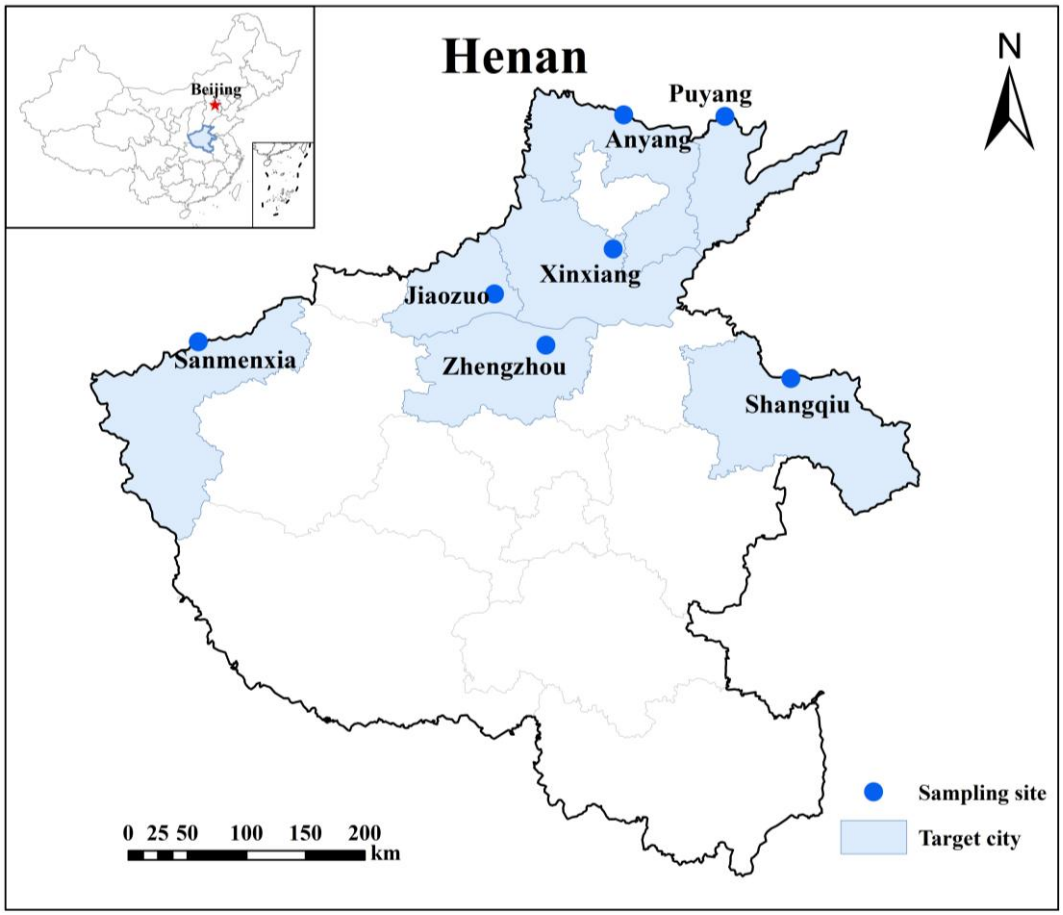

Figure S1. Sampling point map in Henan Province, China. © 2024 National Geomatics Center of China.

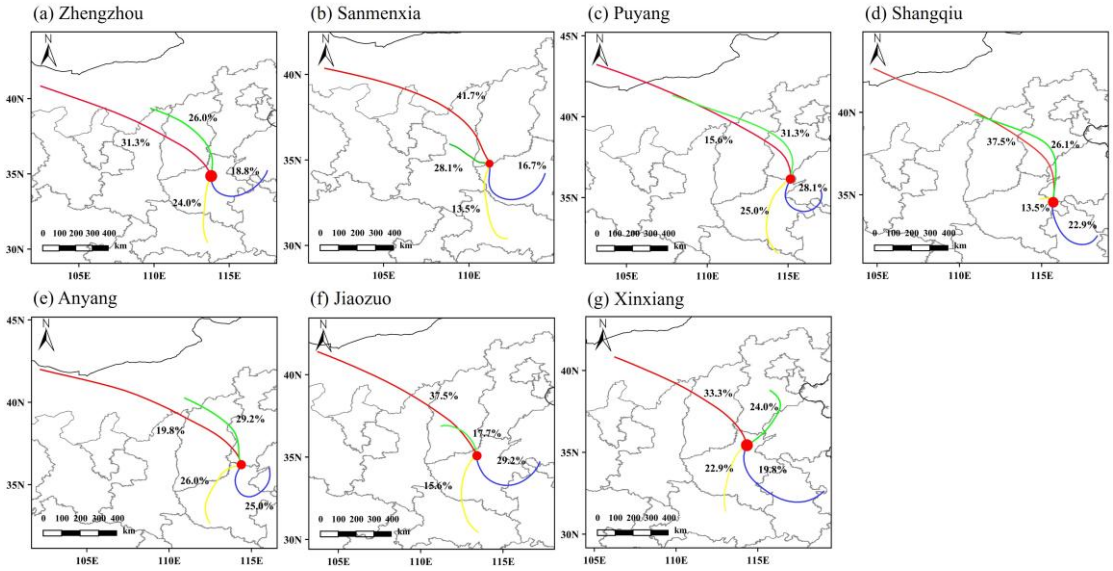

Figure S2. Backward air-mass trajectories during the dust pollution episode from 7 to 17 April 2023 in Zhengzhou (a), Sanmenxia (b), Puyang (c), Shangqiu (d), Anyang (e), Jiaozuo (f), and Xinxiang (g).

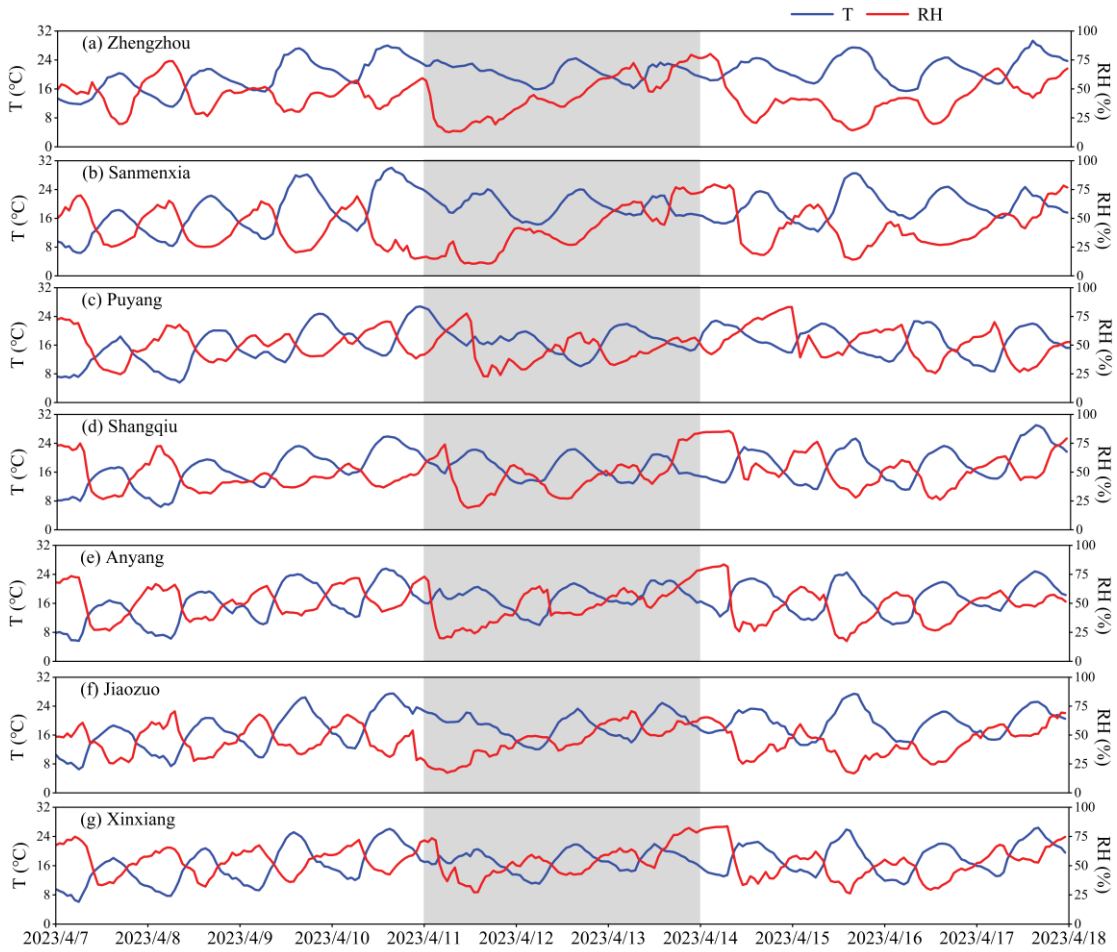

Figure S3. Time series of relative humidity (RH) and temperature (T) in each city during the observation period. The shaded area denotes the dust pollution episode.

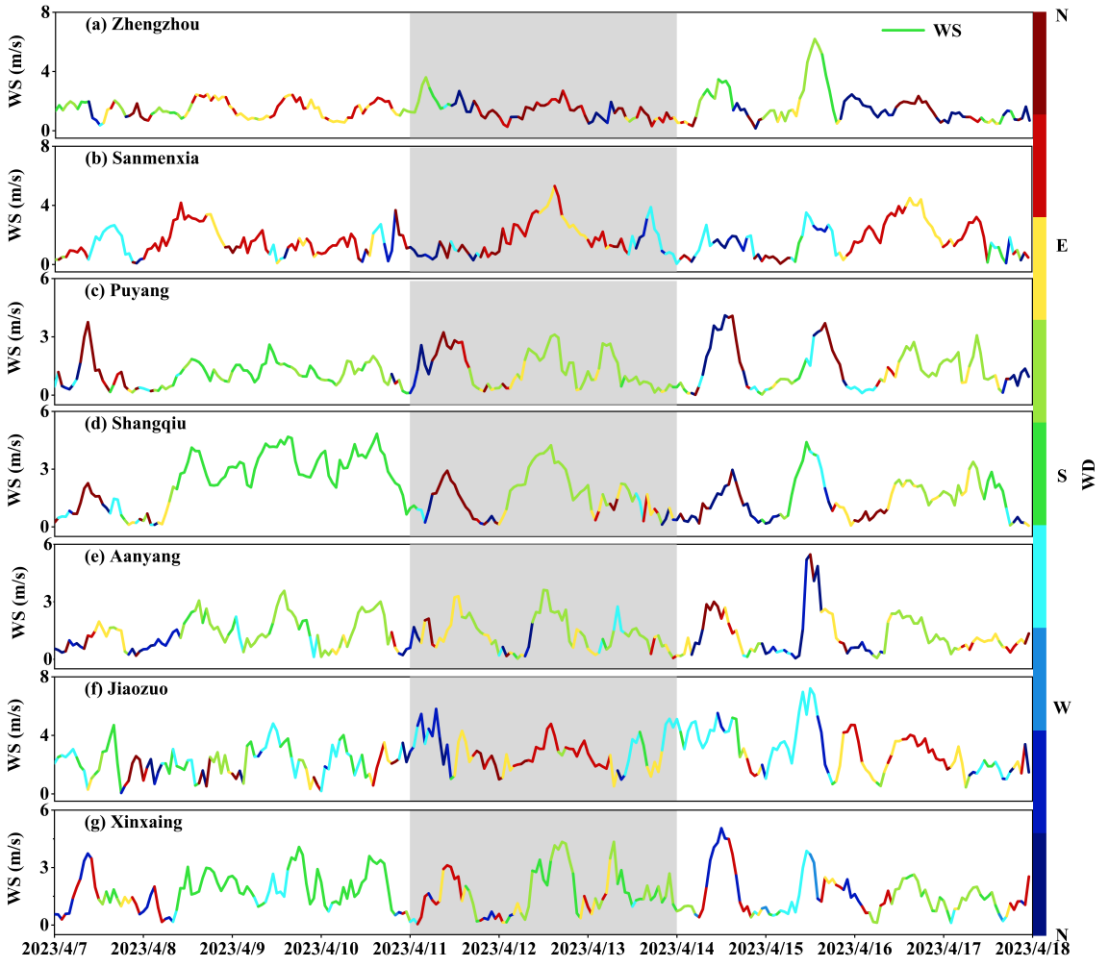

Figure S4. Temporal variations in wind speed and direction across the cities during the observation period. The shaded area indicates the dust pollution episode.

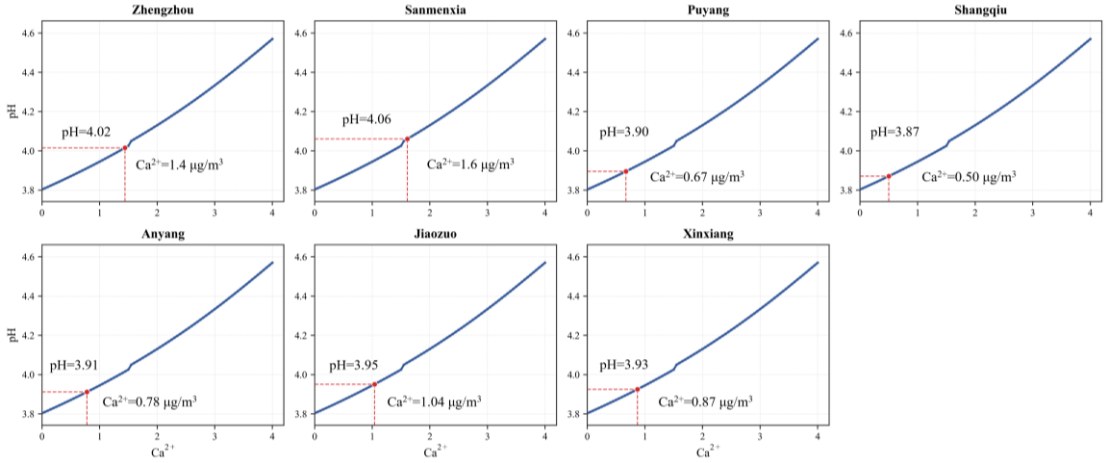

Figure S5. Sensitivity analysis of particle pH to variations in Ca^{2+} concentration.

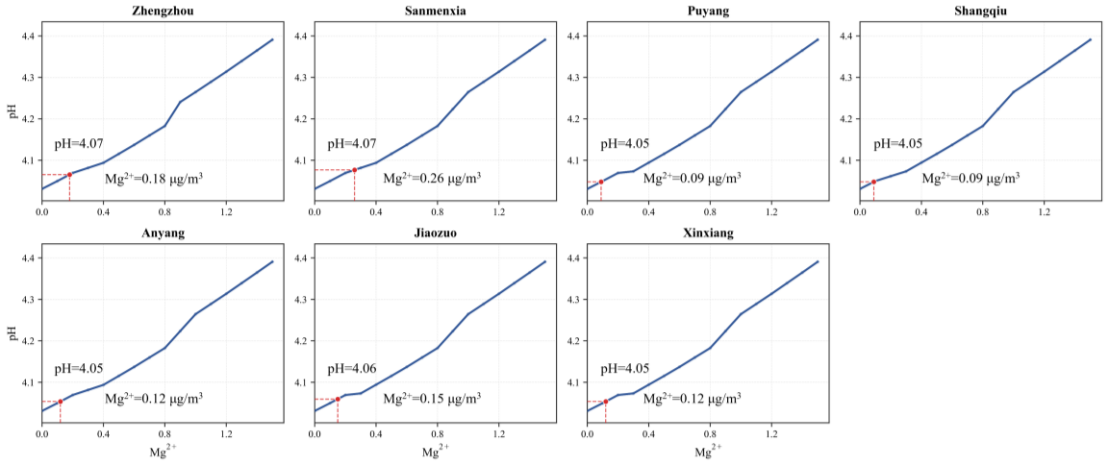

Figure S6. Sensitivity analysis of particle pH to variations in Mg^{2+} concentration.

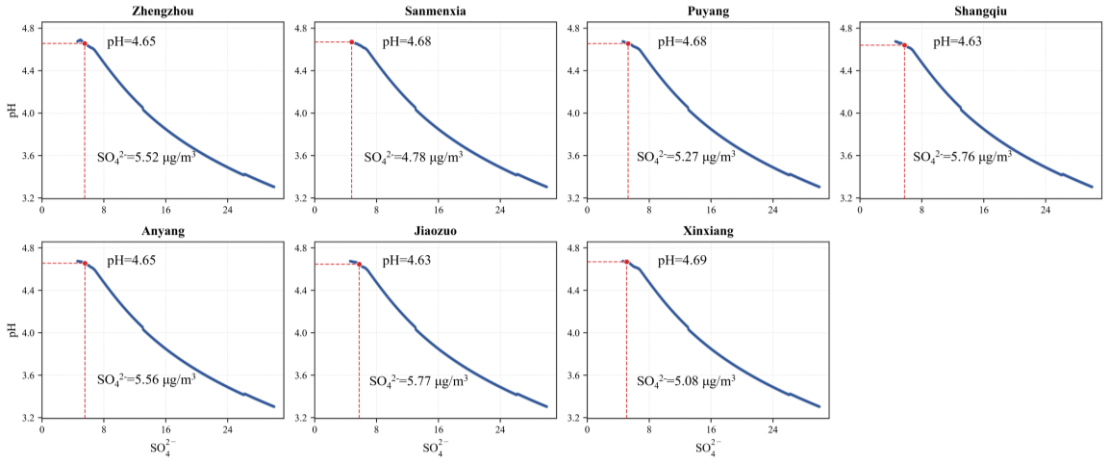

Figure S7. Sensitivity analysis of particle pH to variations in SO_4^{2-} concentration.

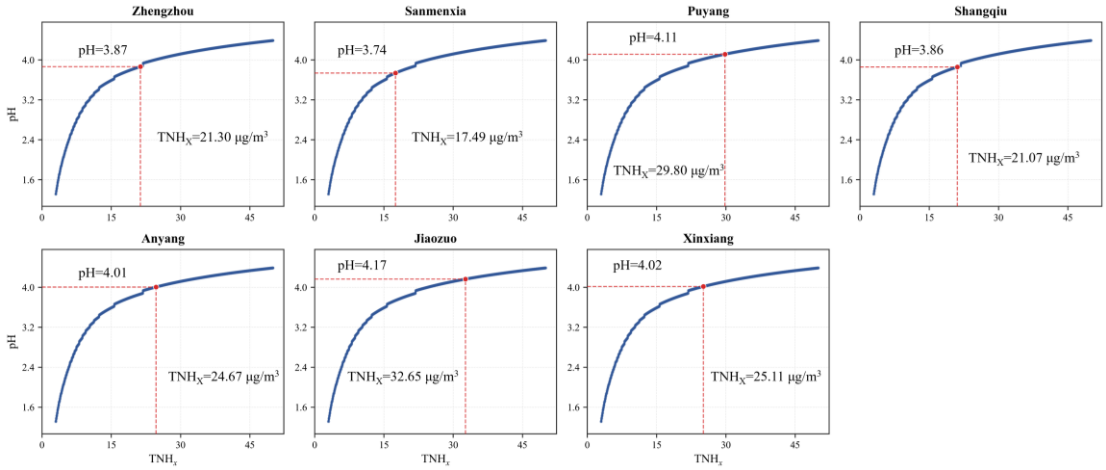

Figure S8. Sensitivity analysis of particle pH to variations in TNH_x concentration.

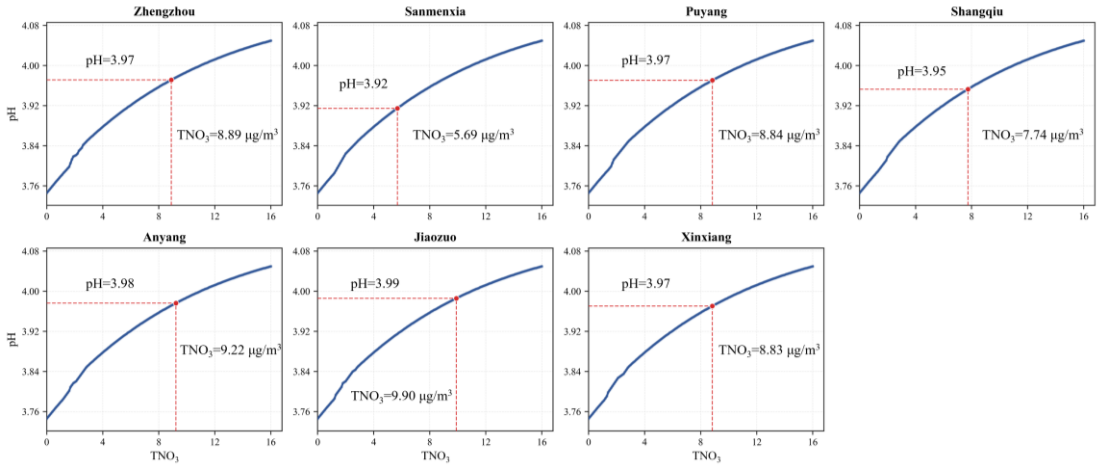

Figure S9. Sensitivity analysis of particle pH to variations in TNO_3 concentration.

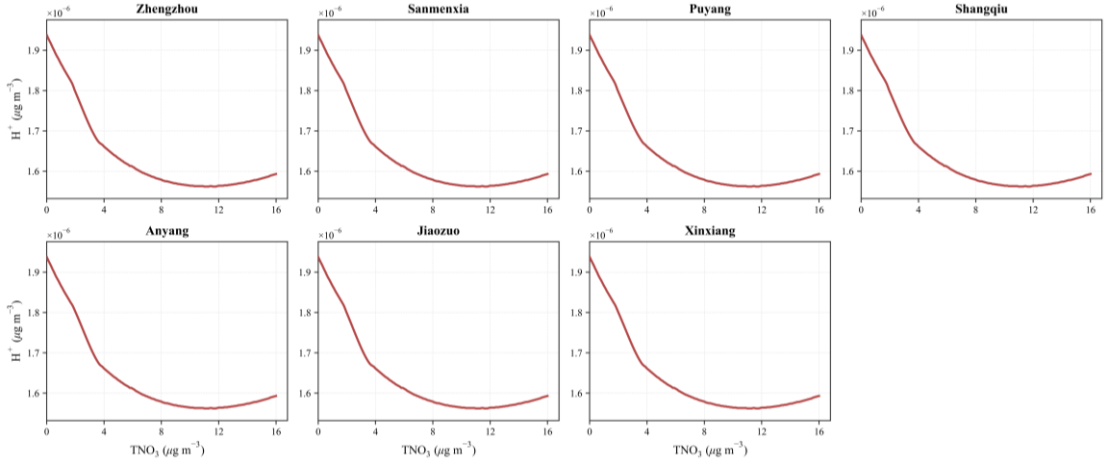

Figure S10. Sensitivity of H^+ concentration to variations in TNO_3 concentration.

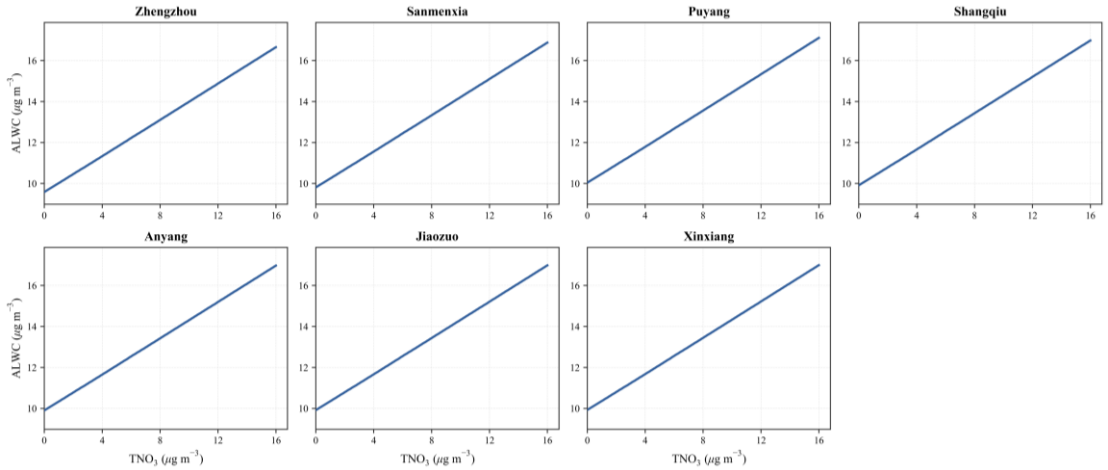

Figure S11. Sensitivity of ALWC concentration to variations in TNO_3 concentration.

Table.

Table S4. Descriptions of the seven sampling sites in Henan Province, China.

Observation sites	Abbreviations	Coordinates	Locations	Surrounding environment
Zhengzhou	ZZ	Department of Ecology and Environment of Henan Province	34.78°N, 113.81°E	Roads, residential areas
Sanmenxia	SMX	Sanmenxia Environmental Protection Bureau	34.80°N, 111.17°E	Roads, residential areas
Anyang	AY	Baizhuang Town Xindian North Street China Resources Gas (Andan Station)	36.21°N, 114.40°E	Highways, villages, farmland
Xinxiang	XX	Banzao Township Central School in Yanjin County	35.38°N, 114.32°E	Villages, farmland
Puyang	PY	Nanle County Longwang Temple Station	36.20°N, 115.17°E	Villages, farmland
Jiaozuo	JZ	The Second River Bureau of Jiefeng Village, Beiguo Township, Wuxi County	35.10°N, 113.42°E	Villages, farmland
Shangqiu	SQ	Liangyuan Huanghe Gudao National Forest Park	34.57°N, 115.67°E	Highways, villages, farmland

References.

Cheng, Y., Zheng, G., Wei, C., Mu, Q., Zheng, B., Wang, Z., Gao, M., Zhang, Q., He, K., and Carmichael, G.: Reactive nitrogen chemistry in aerosol water as a source of sulfate during haze events in China. Sci. Adv., 2, e1601530, 2016.

Healy, R. M., Sciare, J., Poulain, L., Crippa, M., Wiedensohler, A., Prévôt, A. S. H., Baltensperger, U., Sarda-Estève, R., McGuire, M. L., Jeong, C.-H., McGillicuddy, E., O'Connor, I. P., Sodeau, J. R., Evans, G. J., and Wenger, J. C.: Quantitative determination of carbonaceous particle mixing state in Paris using single-particle mass spectrometer and aerosol mass spectrometer measurements, Atmos. Chem. Phys., 13, 9479–9496, 2013.

Li, Y. J., Sun, Y., Zhang, Q., Li, X., Li, M., Zhou, Z., and Chan, C.K.: Real-time chemical characterization of atmospheric particulate matter in China: A review, Atmos. Environ., 158, 270–304, 2017.

Liu, J., Bergin, M., Guo, H., King, L., Kotra, N., Edgerton, E., Weber, R. J.: Size-resolved measurements of brown carbon in water and methanol extracts and estimates of their contribution to ambient fine-particle light absorption. Atmos. Chem. Phy., 13, 12389−12404, 2013.

Markovic, M. Z., Vandenboer, T. C., Murphy, J. G.: Characterization and optimization of an online system for the simultaneous measurement of atmospheric water-soluble constituents in the gas and particle phases. J Environ. Monitor., 14, 1872−1884, 2012.

Panteliadis, P., Hafkenscheid, T., Cary, B., Diapouli, E., Fischer, A., Favez, O., Quincey, P., Viana, M., Hitzenberger, R., Vecchi, R.: ECOC comparison exercise with identical thermal protocols after temperature offset correction: instrument diagnostics by in-depth evaluation of operational parameters. Atmos. Meas. Tech., 8, 779−792, 2014.

Rumsey, I. C., Cowen, K. A., Walker, J. T., Kelly, T. J., Hanft, E. A., Mishoe, K., Rogers, C., Proost, R., Beachley, G. M., Lear, G.: An assessment of the performance of the Monitor for AeRosols and GAses in ambient air (MARGA): a semi-continuous method for soluble compounds. Atmos. Chem. Phy., 14, 5639−5658, 2014.

Seinfeld, J. H., and Pandis, S. N. Atmospheric Chemistry and Physics: From Air Pollution to Climate Change, 2nd Edition: Welly, 2006.

Shi, G., Xu, J., Peng, X., Xiao, Z., Chen, K., Tian, Y., Guan, X., Feng, Y., Yu, H., Nenes, A.: pH of aerosols in a polluted atmosphere: source contributions to highly acidic aerosol. Environ. Sci. Technol., 51, 4289−4296, 2017.

Wang, S., Yin, S., Zhang, R., Yang, L., Zhao, Q., Zhang, L., Yan, Q., Jiang, N., and Tang, X.: Insight into the formation of secondary inorganic aerosol based on high-time-resolution data during haze episodes and snowfall periods in Zhengzhou, China. Sci. Total Environ.,

660, 47–56, 2019.

Song, S., Gao, M., Xu, W., Shao, J., Shi, G., Wang, S., Wang, Y., Sun, Y., Mcelroy, M. B.: Fine particle pH for Beijing winter haze as inferred from different thermodynamic equilibrium models. Atmos. Chem. Phy., 18, 7423−7438, 2018.

VandenBoer, T. C., Markovic, M. Z., Sanders, J. E., Ren, X., Pusede, S. E., Browne, E. C., ... & Murphy, J. G.: Evidence for a nitrous acid (HONO) reservoir at the ground surface in Bakersfield, CA, during CalNex 2010. J. Geophy. Res.: Atmos., 119(14), 9093-9106, 2014.